INSTITUTE OF PHYSICS PUBLISHING PLASMA SOURCES SCIENCE AND TECHNOLOGY

Plasma Sources Sci. Technol. **15** (2006) 735–743 doi:10.1088/0963-0252/15/4/018

Study of control parameters for separation mitigation using an asymmetric single dielectric barrier plasma actuator

K P Singh[1,3], Subrata Roy[1] and Datta V Gaitonde[2]

[1] Computational Plasma Dynamics Laboratory, Mechanical Engineering, Kettering University, Flint, Michigan 48504, USA
[2] Computational Sciences Branch, Air Vehicles Directorate, Air Force Research Laboratory, Wright Patterson AFB, Ohio 45433, USA

E-mail: ksingh@kettering.edu

Received 9 December 2005, in final form 23 July 2006
Published 22 August 2006
Online at stacks.iop.org/PSST/15/735

Abstract
Separation mitigation using asymmetric dielectric barrier discharges is studied by considering the neutral gas flow past a flat plate at an angle of attack. A self-consistent plasma actuator model is employed to couple the electric force field to the momentum of the neutral gas. The equations governing the motion of electrons, ions and neutrals are solved with Poisson's equation to study effective control of flow separation. The impact of select parameters such as amplitude of the excitation, dielectric constants, the initial ionization level and the electrode shape is elucidated. It is found that the dielectric surface just downstream of the exposed electrode becomes negatively charged during part of the cycle for the chosen work parameters and a time averaged force acts on the plasma predominantly downstream, with a transverse component towards the wall. The momentum of the plasma couples to neutral gas through collisions, which results in the enhancement of near-wall momentum yielding a wall-jet feature that effectively eliminates the separation bubble.

(Some figures in this article are in colour only in the electronic version)

1. Introduction

Active flow control is useful for various applications. For example, in propulsion, low-pressure turbines use highly loaded airfoils to improve efficiency and to reduce the number of blades required. The boundary layers, which are fully turbulent at take off, become transitional at high altitudes because of the change in operating environment at cruise [1]. Under such off-design conditions, separation can occur and performance may be impaired. Similarly, in external aerodynamics, the maximum lift and stall characteristics of a wing affect take off and landing distance, maximum and sustained turn rates, climb and glide rates and flight ceiling. Clearly an efficient passive [2] or active device [3, 4] is required to mitigate performance deficiencies encountered in many practical applications at off-design conditions. Plasma-based actuators exhibit several potential benefits in flow control applications, including absence of moving parts, rapid on-off deployment and attractive self-limiting characteristics. In recent years, experimental observations have shown the capability of dielectric barrier devices, operating at relatively low power levels, to suppress separation in a wide range of applications even at atmospheric pressures [5, 6]. The discharge may be characterized as a transient microdischarge and the time scale for the discharge is an order of microsecond and that for the neutral gas is a millisecond.

Recent studies have demonstrated the capability of plasma discharges in promoting boundary layer attachment on airfoils

[3] Author to whom any correspondence should be addressed.

 © 2006 IOP Publishing Ltd Printed in the UK

at a high angle-of-attack. Plasma discharge accomplishes this by supplying additional momentum to the boundary layer and is effective at atmospheric pressures. Baird *et al* [7] have carried out acoustic testing of the dielectric barrier discharge plasma actuator. Their results suggest that compressibility effects may play an important role in the momentum coupling between plasma and neutral gas. The use of a plasma actuator for a variety of flow control applications and its design has been studied [8]. The body force per unit volume of plasma has been used in numerical simulations. Different models for dependence of the volume of plasma on input voltage, frequency and electrode geometry have also been developed and used to further optimize actuator performance. Particle-in-cell and Monte-Carlo (PIC-DSMC) methods have been utilized for computational study of the plasma discharge and its interaction with the flow [9]. The plasma composition, its physics of generation and methods of momentum coupling to neutral gas have been studied. They found that ionization is not equal during both cycles, which results in the plasma actuator producing a net force in one direction. The body forces originating from radio-frequency asymmetric dielectric barrier-discharge actuators have been calculated using direct numerical simulations [10] and the response of the flow past a stalled NACA 0015 airfoil at 15° angle of attack and Reynolds number of 45,000 have been found out.

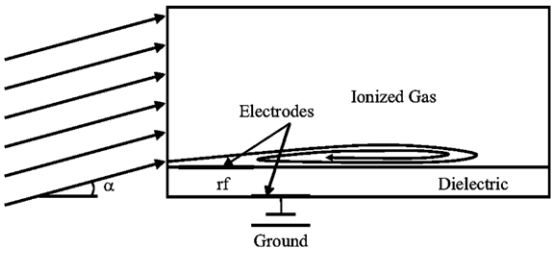

Figure 1. Schematic of an asymmetric single dielectric barrier plasma actuator with an incident gas flow angle α. The domain is 10 cm long and 5 cm high, dielectric thickness is 0.1 cm. The rf electrode extends from $x = 0.3$ cm to $x = 1.5$ at $y = 0.1$ cm, the grounded electrode is from 1.48 to 2.75 cm at $y = 0$.

The force per unit volume acting on the flow and due to the momentum transfer from charged particles to neutral molecules has been calculated using a two-dimensional fluid model of the surface discharge. The force in the DBD was found to be of the same nature as the electric wind in a corona discharge and localized in the cathode sheath region of the discharge expanding along the dielectric surface [11]. The asymmetric surface dielectric barrier discharge in atmospheric air has been used experimentally for airflow production close to the dielectric surface. The time-averaged flow velocity spatial profiles has been found with velocities of up to 3.5 ms^{-1} at heights of 1–2 mm. The effect of several discharge parameters such as applied voltage waveform, distance between electrodes, dielectric thickness and permittivity has been determined [12]. The measurements of the instantaneous flow velocity induced by surface plasma actuators in air at atmospheric pressure have been conducted with two different types of plasma actuators in order to determine the establishment time of the induced airflow. A

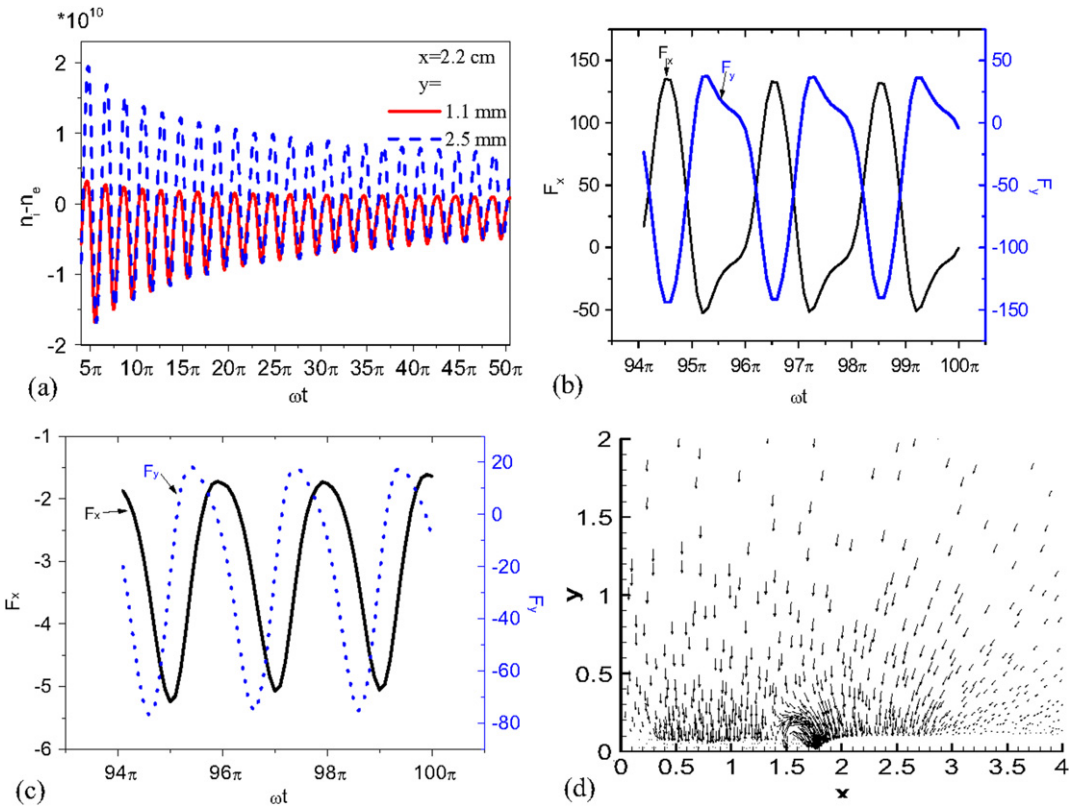

Figure 2. (*a*) Variation in charge separation $(n_i - n_e)$ as a function of normalized time ωt at $x = 2.2$ cm for $y = 1.1$ and 2.5 mm. The force per unit volume $e(n_i - n_e)\boldsymbol{E}$ (dyne cm^{-3}) components as function of ωt at (*b*) $x = 1.75$ cm and $y = 0.25$ cm, and (*c*) $x = 2.5$ cm and $y = 0.25$ cm (*d*) Time-averaged force distribution. x and y are in cm.

strong correlation was found between the transient regime of the discharge current and the ionic wind velocity. The AC discharge was found to induce a pulsed airflow at a frequency corresponding to the high voltage waveform frequency and the DC discharge airflow with important fluctuations [13]. The performance of plasma actuators has been studied with wind tunnels, drag balances, Pitot tubes, smoke flow visualization and fluid dynamic modelling programs. The power couples to the neutral gas flow by ion-neutral collisions. The power flows by adjustment of the actuator geometry, materials, the RF frequency and RMS voltage have been studied [14].

The present authors have carried out a simulation study of an asymmetric single dielectric barrier plasma actuator [15, 16]. The equations governing the dynamics of electrons and ions has been solved to obtain spatio-temporal profiles of electron density, ion density and electric potential. For various electrical and geometric parameters, the solutions demonstrate the dominance of the electrohydrodynamic force is in the positive direction during the rf cycle. The dielectric surface above the grounded electrode behaves as a virtual negative electrode during the majority of the cycle. In this paper, we study active separation control using an asymmetric dielectric barrier plasma actuator. We solve the equations governing the dynamics of electrons, ions and fluid to obtain spatio-temporal profiles of electron density, ion density, electric potential, neutral gas density and neutral gas velocity. The parameters controlling the force are the dielectric characteristics, applied voltage, frequency, the asymmetric configuration of the electrodes and the, thickness of the exposed electrode. We have found effects never reported in the literature which may lead to new experimental investigations.

2. Actuator physics description

Figure 1 shows the schematic of an asymmetric single dielectric barrier plasma actuator. It consists of two electrodes separated by a dielectric. The upper electrode is exposed to the free stream flow while the lower electrode is placed underneath the dielectric. The two electrodes overlap horizontally with each other. The region simulated is 10 cm long and 5 cm high. The lower part of the domain consists of a 0.1 cm thick insulator with a dielectric constant $\varepsilon_d = a\varepsilon_0$ while the upper part is filled with inert helium gas of $\varepsilon_f = 1.0055\,\varepsilon_0$, where ε_0 is permittivity of the free space. In real aerodynamic applications, air may be the working gas in place of helium. This will affect the chemistry of ion formation. We have chosen helium for simplicity. The charged particles will play a major role in either case in producing a directional body force. The thickness of the electrodes is assumed to be infinitesimally small. The rf electrode extends from $x = 0.3$ cm to $x = 1.5$ cm at $y = 0.1$ cm, the grounded electrode is from 1.48 to 2.75 cm at $y = 0$, with a 0.02 cm overlap between the electrodes along the x-axis. The embedded electrode is grounded and a sinusoidal voltage $\phi = \phi_0 \sin(2\pi f t)$ is applied to the exposed electrode. The frequency of excitation is fixed at $f = 5$ kHz. Theinitial velocity components u_0 (along the x-direction) and v_0 (along the y-direction) are 1000 cm s^{-1} and 175 cm s^{-1}, respectively, corresponding to an angle of attack (α) of approximately 10°. The separated region observed in the vicinity of the leading edge of the plate is then subjected to control with a suitably placed asymmetric single dielectric barrier plasma actuator.

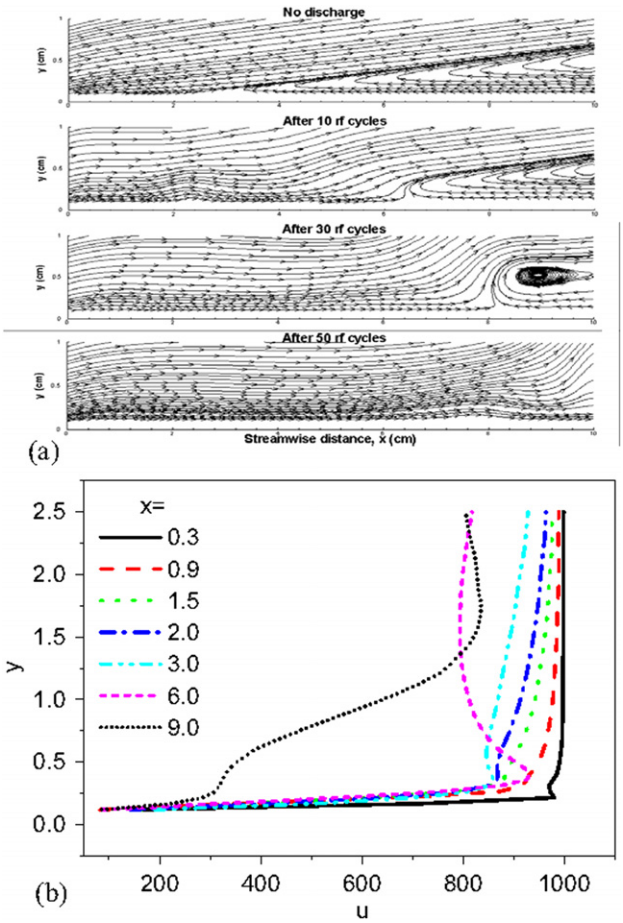

Figure 3. (a) Streamlines and vectors of gas velocity at the end of 1 s, 10, 30 and 50 cycles. (b) Gas velocity components u (in cm s^{-1}) as a function of y (in cm). x is in cm.

The drift–diffusion form of continuity and Poisson's equations for the electrons and ions are solved as described in [15, 16] together with the following fluid momentum and continuity equations:

$$\frac{\partial n_\alpha}{\partial t} + \nabla(n_\alpha \boldsymbol{v}_\alpha) = n_e S, \qquad \alpha = e, i \tag{1a}$$

where $n_\alpha \boldsymbol{v}_\alpha = n_e \mu_e \nabla\phi - D_e \nabla n_e$ for electrons and $n_\alpha \boldsymbol{v}_\alpha = -n_i \mu_i \nabla\phi - D_i \nabla n_i$ for ions

$$\varepsilon \nabla^2 \phi = e(n_e - n_i), \tag{1b}$$

$$\rho \frac{\partial \boldsymbol{u}}{\partial t} - \nabla(\eta \nabla \boldsymbol{u}) + \rho(\boldsymbol{u} \cdot \nabla)\boldsymbol{u} + \nabla p = e(n_e - n_i)\nabla\phi, \tag{2a}$$

$$\frac{\partial \rho}{\partial t} + \nabla(\rho \boldsymbol{u}) = 0, \tag{2b}$$

where n_e, n_i, ρ, $\boldsymbol{v}_e$, $\boldsymbol{v}_i$ and $\boldsymbol{u}$ are densities and velocities of electrons, ions and the working gas, respectively, η is the gas viscosity, S is the Townsend ionization rate, pressure $p = \rho RT/M$, M (mole/gm) is the molar mass of helium, T is the temperature (300 K), R is the universal gas constant (erg/(mole K)). The bulk density of the helium is taken to be 1.79×10^{-4} g cm^{-3}, and the viscosity is assumed to be 1.9 P.

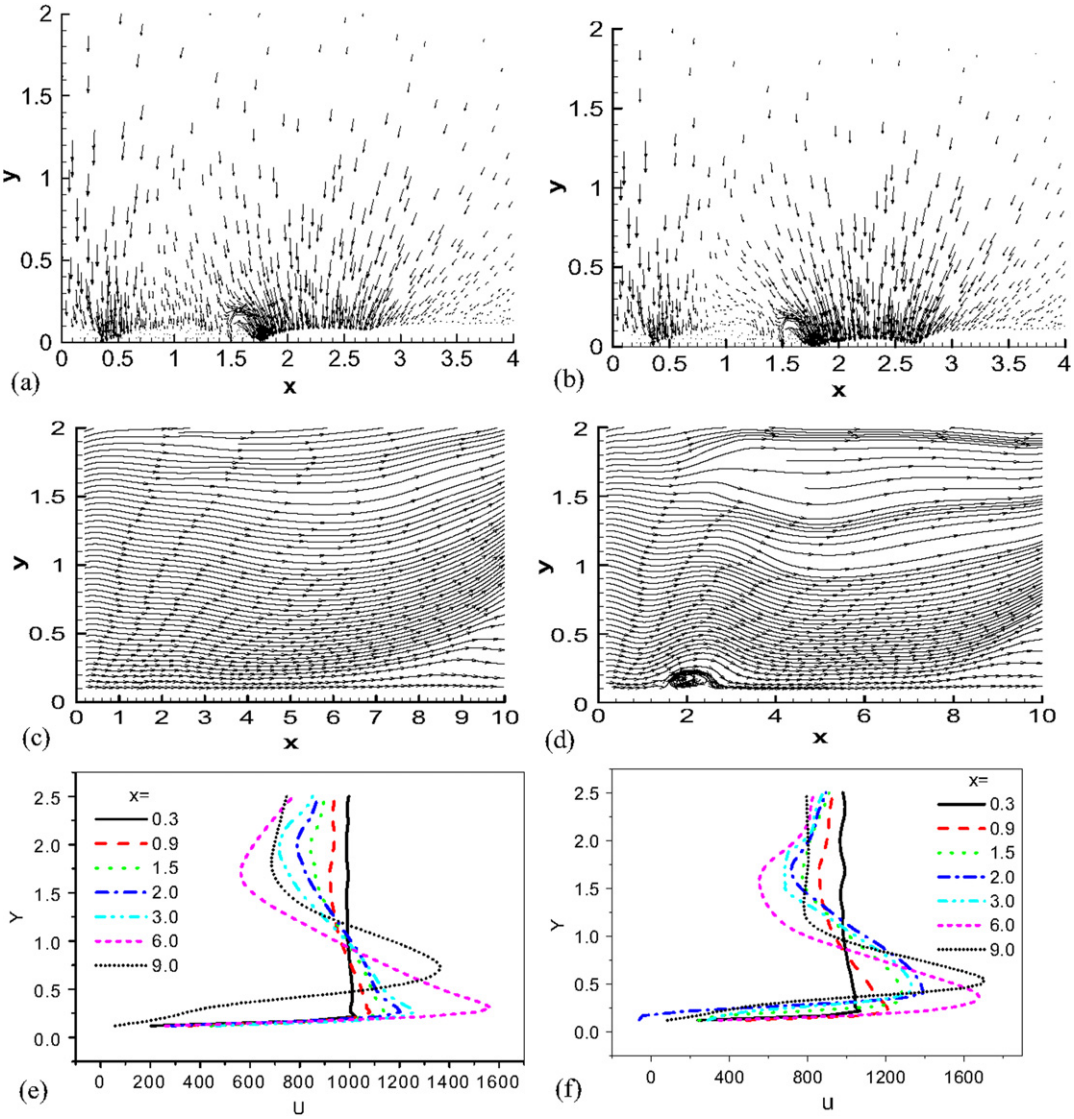

Figure 4. (*a*) and (*b*) vectors of time-averaged force distribution, (*c*) and (*d*) streamlines and vectors of gas velocity and (*e*) and (*f*) gas velocity components u (in cm s^{-1}) as a function of y for initial plasma density 5×10^{10} cm^{-3} and 1×10^{11} cm^{-3} , respectively. x and y are in cm.

The mobilities μ_α and diffusion rates D_α are taken from [15]. The self-consistent formulation is solved using a Galerkin variational formulation based finite-element method [17] to obtain electron and ion density, electric potential, neutral velocity and density. The no-slip condition is assumed for the gas neutrals at the dielectric surface and the velocity at the left boundary of the upper domain is set to the freestream condition at all times. Homogeneous Neumann conditions for the normal component of electron and ion currents and the normal component of the electric field are applied to the all the outer boundaries of the domain except the grounded electrode. The electron and ion currents flow only normal to the rf electrode and normal as well as parallel to dielectric surface because rf electrode is an equipotential surface ($E_x = 0$), dielectric surface is not. Charge density inside the dielectric is zero, hence, the normal electron and ion currents are discontinuous across the plasma and dielectric boundaries by $-en_e\mu_e E_y$ and $en_i\mu_i E_y$, respectively. The normal component of the electric field is discontinuous by $e(n_i - n_e)$ (derived from Poisson's equation). Thus the total current continuity is automatically ensured across the dielectric interface i.e. at this location, conduction, convection and displacement currents in the gas are balanced with the displacement current in the dielectric.

3. Results and discussion

We have studied a total of nine cases. We have chosen $n_0 = 10^{10}$ cm^3, $a = 3.5$, $\phi_0 = 400$ volts and negligible rf electrode thickness for the reference case. Since the gas is pre-ionized a reasonably small rf potential is assumed sufficient to maintain the discharge. For other cases the amplitude of rf voltage ϕ_0, initial plasma density n_0, dielectric constant a or rf electrode shape are varied to see the effect of change in the parameters.

The electrons are repelled by the insulated electrode and by the exposed electrode during the positive and the negative part of the rf voltage, respectively. The electrons are absorbed at the surface of the rf electrode during the positive part of the

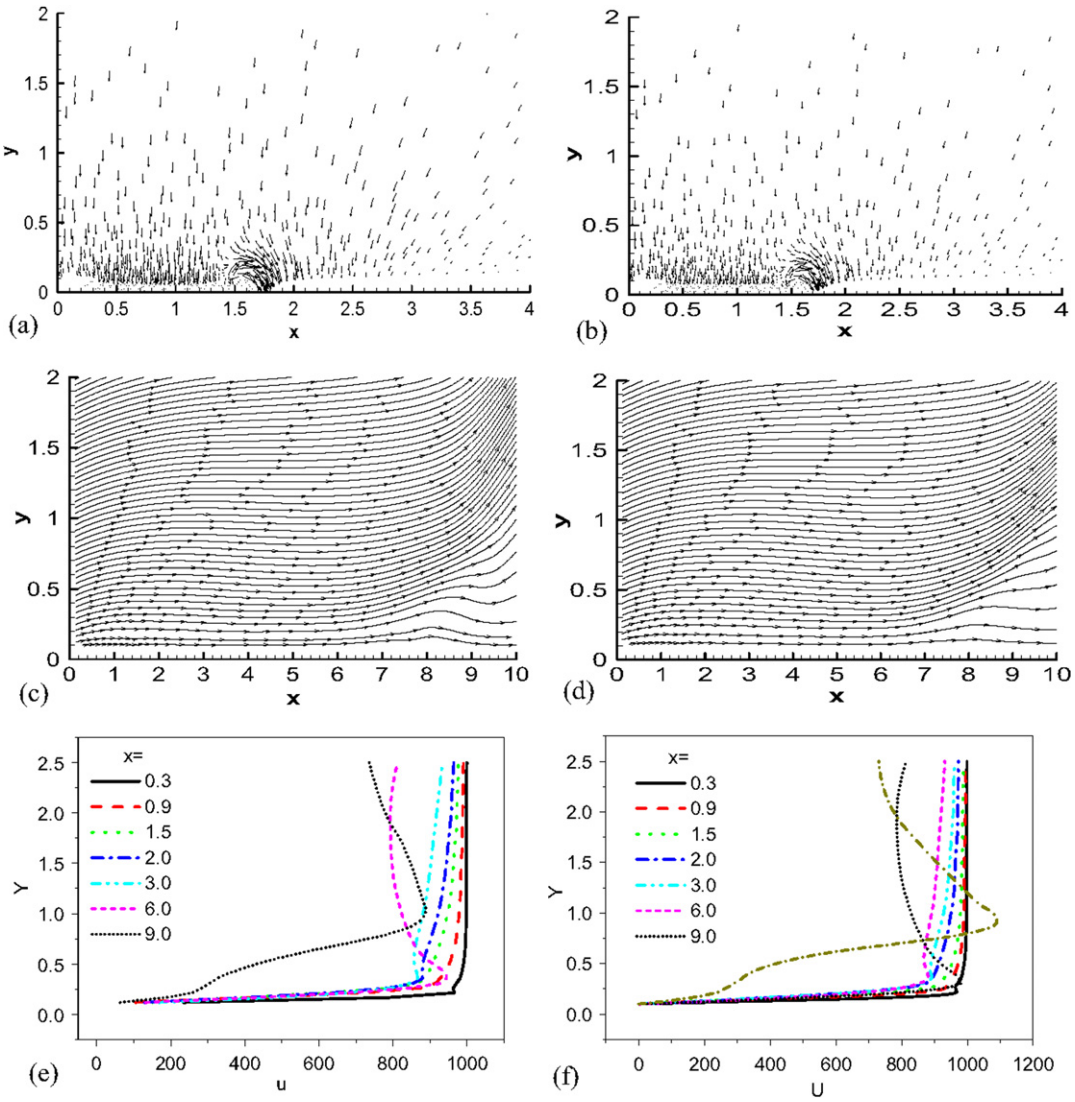

Figure 5. (*a*) and (*b*) vectors of time-averaged force distribution, (*c*) and (*d*) streamlines and vectors of gas velocity and (*e*) and (*f*) gas velocity components u (in cm s^{-1}) as a function of y for dielectric constant $\varepsilon = 7$ and $\varepsilon = 14$, respectively.

cycle; however, during the negative part the cycle, electrons get deposited at the surface of the dielectric above the grounded electrode. The dielectric surface becomes negatively charged. Figure 2(*a*) shows a variation in charge separation $(n_i - n_e)$ as a function of normalized time ωt at $x = 2.2$ cm for $y = 1.1$ and 2.5 mm. The value of $(n_i - n_e)$ is negative except near the positive peak of the cycle for $y = 1.1$ mm which implies electron deposition at this point. The value of $(n_i - n_e)$ is positive for $y = 2.5$ mm except near the negative peak of the cycle which implies ion density is higher than that of electron density at this point for most of the time. The solution approaches steady-state after 20 cycles. The local imbalance arising from the different mobilities of the ions and electrons results in a time-varying charge separation distribution and establishment of a consistent electric field. The electric field $\boldsymbol{E}$ exerts a net force $\boldsymbol{F} = e(n_i - n_e)\boldsymbol{E}$ on the space charge separated plasma. At all phases in the cycle, the peak magnitude of the force is located downstream of the rf electrode. Figures 2(*b*) and (*c*) plot the calculated forces per unit volume $e(n_i - n_e)\boldsymbol{E}$, as function of ωt at $x = 1.75$ cm and $y = 0.25$ cm and $x = 2.5$ cm and $y = 0.25$ cm, respectively. For figure 2(*b*), the x-component of the force takes both positive and negative values during the positive and negative parts of the cycle, respectively; its magnitude during the former phase is nearly thrice larger than in the latter (cf [18]). The y-component of the force is negative during most of the cycle, becoming marginally positive only at the negative peak of the voltage. The magnitude of both forces is the highest around the positive peak of the cycle and almost zero at the end of the cycle. The time average of the force at this point is oriented in the positive x and negative y-direction. For figure 2(*c*), the x-component of the force takes both positive and negative values during the positive and negative parts of the cycle, respectively. Its magnitude during the former phase is lower than in the latter. The time average of the force at this point is oriented in the negative-x and negative y-direction. The magnitude of the x-component of the force in figure 2(*b*) is higher than that in figure 2(*c*); therefore net force is in the positive x-direction. Figure 2(*d*) shows a vector plot of the time average of the force. It can be seen that arrows are directed towards the

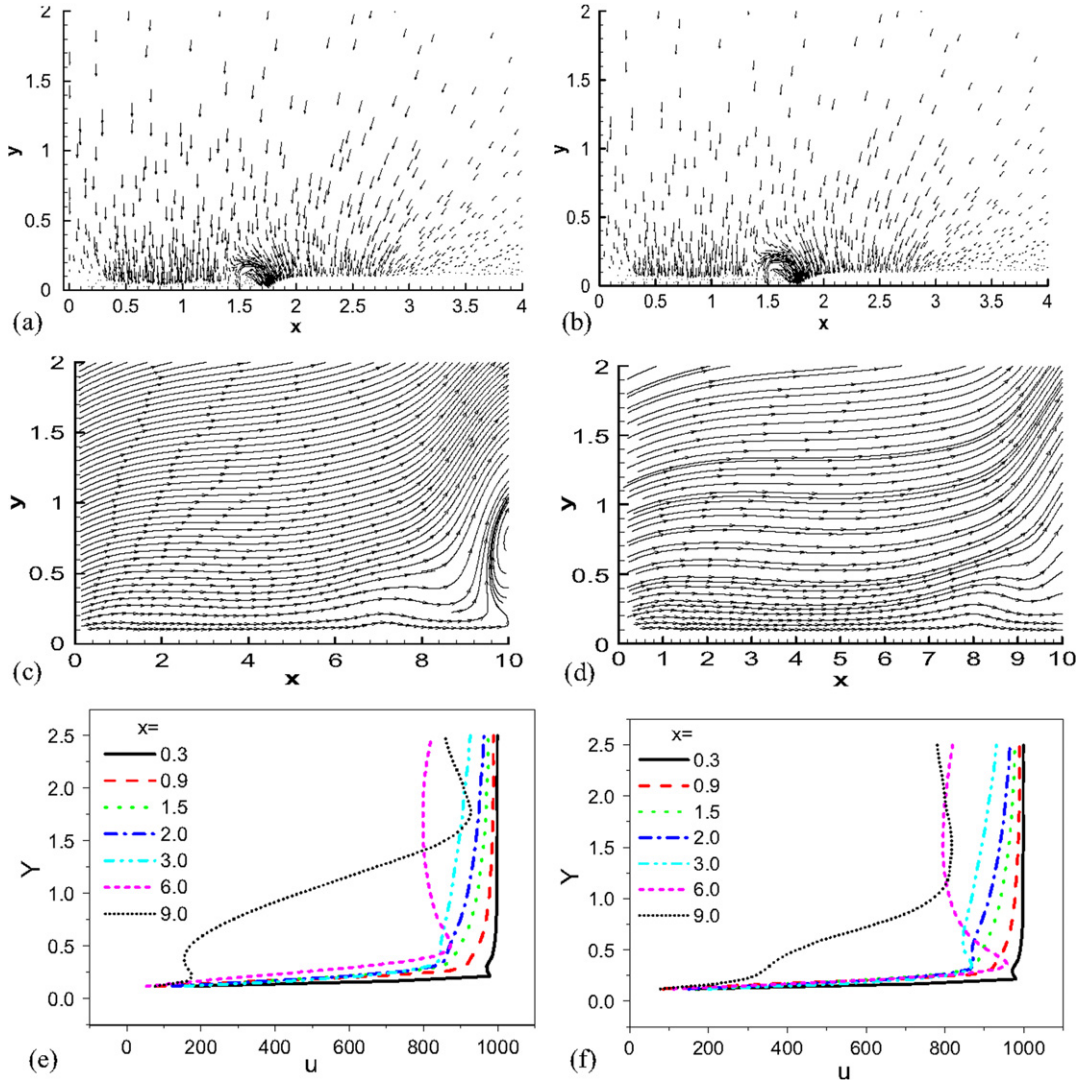

Figure 6. (*a*) and (*b*) vectors of time-averaged force distribution, (*c*) and (*d*) streamlines and vectors of gas velocity and (*e*) and (*f*) gas velocity components u (in cm s^{-1}) as a function of y for $\phi_0 = 300$ volts and $\phi_0 = 450$ volts, respectively.

downstream region from both the positive-x and the negative-x directions. It can be seen again that the magnitude of the positive-x force is larger than that of the negative-x force. The electric field $\boldsymbol{E}$ is directed from the rf electrode to the grounded electrode and the force on the charge separation also follows the electric lines of force. This explains the things about time average of the force. The plasma is highly collisional, which results in energy exchange between the charged and neutral species. Consequently, collision effects ensure that the dominant neutral species experience an accelerating body force downstream and towards the dielectric surface. Since fluid cannot penetrate the dielectric, it is turned parallel to the surface of the dielectric. The net effect as discussed further below is, therefore a gradual mitigation of flow separation. Ensuring the proper magnitude and direction of the time averaged force is key to the successful application of DBD for an actuating effect at higher neutral gas speeds.

The effect of the DBD is highlighted by considering the flow field. The initial field, without the plasma actuator, is shown in the first frame of figure 3(*a*), which depicts the streamline pattern and neutral velocity vector at 1 s (1000 times the characteristic flow timescale) after initiation of the flow. A separation bubble develops near the surface of dielectric—in a practical situation this phenomenon degrades performance through impact on drag or control surface effectiveness. When the plasma actuator is switched on, a highly transient process is initiated as shown in the last three frames of figures 3(*a*), which depict streamlines and vectors of neutral velocity after 10 cycles, 30 cycles, and 50 cycles, respectively. The attachment process downstream of the rf electrode progresses successively downstream: the attachment point is at 6.5 cm after 10 cycles, moving to 8 cm after 30 cycles and finally beyond the computational domain after 50 cycles. This is consistent with the above observation that the net force on the plasma operates downstream of the rf electrode in the positive-x direction. The transfer of momentum results in a near-wall energized flow of neutrals, altering the dynamics of the inertial and adverse pressure gradient terms to eliminate the separation bubble. The neutral density is nearly 10^7 times higher than that of the plasma, which is reflected in the time taken to attach the flow over full length of the dielectric. Figure 3(*b*) shows u-velocity as a function of y for $x = 0.3$, 0.6, 0.9, 1.5, 2,

3, 6 and 9 cm after 50 cycles. The streamwise velocity is nearly zero near the dielectric surface at the end of domain and its value increases with increasing y, i.e. as we move away from the dielectric surface. The wall jet formation is clearly observed within a few mm above the no-slip wall (cf 4,5,6,8,15 and 18). As observed in [15, 18], the wall jet velocity is maximum at a downstream location than the force peak which occurs about the overlap region.

The effect of initial plasma density, dielectric constant, excitation potential and rf electrode shape have been explored in figures 4–7. Parts (a) and (b) of each figure show the time average of the force control of which is in the flow control. Parts (c) and (d) of each figure show arrows and streamlines of neutral velocity which are the consequence of the force operating on the charge separation and give us information about the fluid effect of the EHD force. Parts (e) and (f) of each figure show velocity u as a function of y which gives us an idea about the numerical variation of the x-component of the velocity in the domain.

Figure 4 shows arrows of the time average of force (parts (a) and (b)), arrows of neutral velocity (parts (c) and (d)) and velocity u as a function of y (parts (e) and (f)) for the initial plasma density of 5×10^{10} cm^{-3} and 10^{11} cm^{-3} respectively. The time average of the force is taken for the 48th to 50th cycle with 20 time points in each cycle. The higher value of the initial density results in larger charge separation and hence a higher generated electrostatic field. Consequently, the larger force $e(n_i - n_e)\boldsymbol{E}$ yields more energetic plasma and neutral velocities. The significant body force component in the negative y direction induces a downward flow together with the wall impermeability condition, which results in a complex nonlinear interaction between the force, inertial and pressure mechanisms, the net result of which is the elimination of separation downstream of the electrode. The flow is smoother for the pre-ionization density of 5×10^{10} cm^{-3} than those for 10^{10} cm^3 and 10^{11} cm^3. The lower force generated for an initial plasma density of 10^{10} cm^3 is not sufficient to eliminate the separation bubble as efficiently as for an initial plasma density of 5×10^{10} cm^3. The force is larger than that required for plasma density of 10^{11} cm^3, which results in the formation of a new (tiny) bubble just downstream of the powered electrode.

Figure 5 compares arrows of time average of force (((a) and (b)), arrows of neutral velocity ((c) and (d)) and velocity u as a function of y ((e) and (f)) for dielectric constant $a = 7$ and 14, respectively. With the increase in dielectric constant, the values of the electric field and charge separation are changed (cf [18]) in such a way that the x-component of the force on the charge separation increases resulting in an increase in the x-component of the induced velocities in figures 5(e) and (f).

Figure 6 shows arrows of the time average of force (a) and (b), arrows of neutral velocity (c) and (d) and velocity u as a function of y (e) and (f) for excitation amplitude $\phi_0 = 300$ V and 450 V, respectively. From the arrow plots of figures 6(a) and (b) it can seen that the force is larger for the $\phi_0 = 450$ V case than that for the $\phi_0 = 300$ V case. A low value of excitation amplitude ϕ_0 results in a low electric field $\boldsymbol{E}$ and a low value of charge separation $n_i - n_e$ and vice versa. The separation is more effectively eliminated for the $\phi_0 = 450$ V case as the value of force $\boldsymbol{F}$ is large. A large force results in a larger value of u also. The effect of excitation amplitude has been further explored in figure 7. Figures 7(a) and (b) show the time averaged force per unit volume $e(n_i - n_e)\boldsymbol{E}$ in the x and y directions, respectively, as a function of x along $y = 0.25$ cm, while the streamwise velocity component is shown in figure 7(c). For all cases, the positive peak of the force is near $x = 1.75$ cm, i.e. just downstream of the trailing edge of the exposed electrode, while the negative peak is near $x = 3$ cm. As ϕ_0 increases by 50%, the streamwise force increases by a commensurate amount. The y-component of the force is negative. The magnitude of both the components

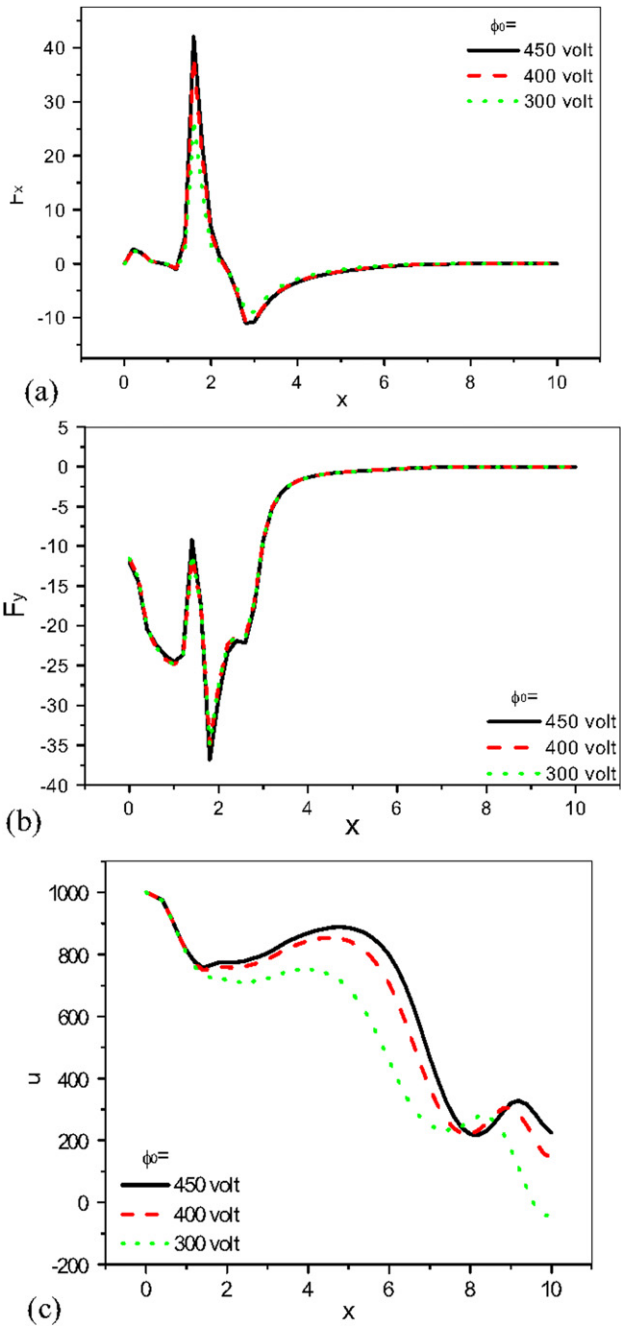

Figure 7. (a) and (b) Time average of the force per unit volume (dyne cm^{-3}) and (c) gas velocity (cm s^{-1}) as a function of x (in cm) for $y = 0.25$ cm for $\phi_0 = 450$, 400 and 300 volts. (d) Velocity u (cm s^{-1}) and the force F_x (dyne cm^{-3}) as a function of rf voltage ϕ_0 (in volts).

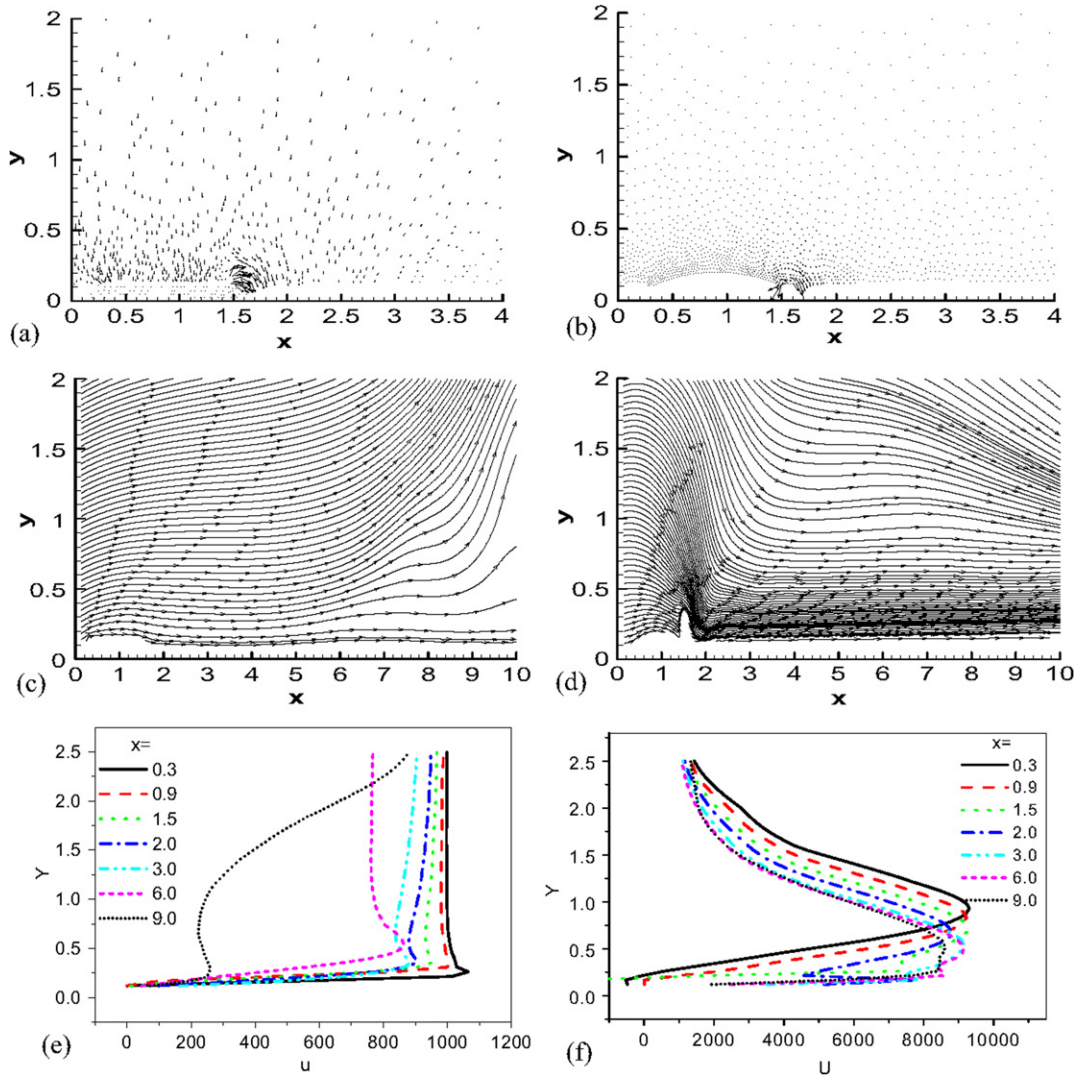

Figure 8. (*a*) and (*b*) vectors of time-averaged force distribution, (*c*) and (*d*) streamlines and vectors of gas velocity and (*e*) and (*f*) gas velocity components u (in cm s^{-1}) as a function of y for finite thickness (0.05 cm) and arcshape rf electrode, respectively.

of the force decreases sharply with y and is negligible beyond $x = 4$ cm.

Figure 8 shows arrows of the time average of force (*a*) and (*b*), arrows of neutral velocity (*c*) and (*d*) and velocity u as a function of y (*e*) and (*f*) for a finite thickness (0.05 cm) and arcshape rf electrode ($x = 0.3$ to 1.5 cm along $y = 0.1$ and height 0.2 cm), respectively. The geometry of this arcshape electrode can be specified by a radius of curvature of 1 cm and angle 73.74°. The velocities are much (nearly eight times) higher in the case of the arcshape rf electrode than these other cases reported in this paper. This may be due to a numerical error that needs to be resolved. However, it is clear that the flow is best attached to the surface for the arcshape rf electrode due to the increase in the x-component of the force $e(n_i - n_e)\boldsymbol{E}$. Figures 8(*a*) and (*b*) demonstrate the effect of the electrode radius of curvature. As the curvature increases, the time-averaged force nearly doubles for an arc shaped electrode with a small radius at the tip. This is in agreement with the experimental observation reported in [6] that the force magnitude increases with the decreasing radius of the electrode. The induced velocities found by us are 1 m s^{-1} to 4 m s^{-1} close to the dielectric surface for different cases. These are of the nearly same magnitude as found by other researchers in [12–14] limited by differences in geometries and parameters.

4. Conclusions

Separation control using an asymmetric dielectric barrier plasma actuator has been studied by considering the neutral gas flow past a flat plate at an angle of attack. A self-consistent plasma actuator model is employed to simulate an atmospheric surface dielectric barrier discharge for partially ionized helium gas. The effect of different parameters on separation control has been illustrated. The equations governing the dynamics of electrons, ions and neutrals are solved using a two-dimensional finite element based formulation of plasma-fluid interactions. The electric field generated due to charge separation is governed by the Poisson equation. Temporal variation of electric field inside the dielectric gives rise to a displacement current. The electrons and ions move in opposite

directions due to the applied driver rf potential. The dielectric surface becomes negatively charged due to electron deposition during part of the cycle and starts behaving as a virtual negative electrode. A time averaged force, predominantly downstream with a transverse component towards the wall, acts on the plasma, which results in an enhancement of near-wall momentum of neutral gas that effectively eliminates the separation bubble. The computed results are similar to the experimental data. The effect of the amplitude of excitation, dielectric constants, the initial ionization level and the electrode shape is found out for the effectiveness of plasma actuators.

Acknowledgments

The work is partially supported by Air Force Research Laboratory contracts and AFOSR grants monitored by John Schmisseur and Rhett Jefferies. The authors acknowledge many thoughtful discussions with Natalia Sternberg (Clark University) and Haribalan Kumar (Kettering University).

References

[1] Mayle R E 1991 *J. Turbomach.***113** 509–37
[2] Van Treuren K W *et al* 2002 *J. Turbomach.* **124** 100
[3] Bons J P, Sondergard R and Rivir R B 2001 *J. Turbomach.* **123** 198
[4] Hultgren L S and Ashpis D E 2002 *Bull. Am. Phys. Soc.* **47** 167
[5] Roth J R 2003 *Phys. Plasmas* **10** 2117
[6] Enloe C L *et al* 2004 *AIAA J.* **42** 595
[7] Baird C, Enloe C L, McLaughlin T E and Baughn J W 2005 *43rd Aerospace Sciences Meeting (Reno, NV, January 10–13 2005)* AIAA-2005-0565
[8] Corke T C and Post M L 2005 *43rd Aerospace Sciences Meeting (Reno, NV, January 10–13 2005)* AIAA-2005-0563
[9] Font G I 2004 *40th AIAA/ASME/SAE/ASEE Joint Propulsion Conf. Exhibit (Fort Lauderdale, Fl, July 2004)*
[10] Gaitonde D V, Visbal M R and Roy S 2005 *36th AIAA Plasmadynamics and Laser Conf. (Toronto, June 2005)* AIAA-2005-5302
Gaitonde D V, Visbal M R and Roy S 2006 *44th AIAA Aerospace Sciences Meeting and Exhibit (Reno, NV, January 9–12 2006)* AIAA-2006-1205
[11] Boeuf J P and Pitchford L C 2005 *J. Appl. Phys.* **97** 103307
[12] Pons J, Moreau E and Touchard G 2005 *J. Phys. D: Appl. Phys.* **38** 3635–42
[13] Forte M, Leger L, Pons J, Moreau E and Touchard G 2005 *J. Electrostat.* **63** 929–36
[14] Roth J R and Dai X 2006 *44th AIAA Aerospace Sciences Meeting and Exhibit (Reno, NV, January 9–12 2006)* AIAA-2006-2103
Roy S *et al* 2006 *44th AIAA Aerospace Sciences Meeting and Exhibit (Reno, NV, January 9–12 2006)* AIAA-2006-0374
[15] Roy S 2005 *Appl. Phys. Lett.* **86** 101502
[16] Singh K P and Roy S 2005 *J. Appl. Phys.* **98** 083303-09
[17] Roy S, Pandey B P, Gaitonde D and Poggie J 2003 *Phys. Plasmas* **10** 2578
[18] Roy S and Gaitonde D 2006 *Phys. Plasmas* **13** 023503